Journal of Materials Chemistry A

Conformal Electrochemical Deposition of Intermetallic AuCu Thin Films for Convergent C-N Coupling

Journal:	*Journal of Materials Chemistry A*
Manuscript ID	TA-ART-10-2024-007268.R1
Article Type:	Paper
Date Submitted by the Author:	27-Nov-2024
Complete List of Authors:	Gerke, Carter; Johns Hopkins University, Department of Chemistry Foley, Gregory ; Johns Hopkins University, Department of Chemistry Wilder, Logan; National Renewable Energy Laboratory Yang, Yuwei; The University of New South Wales, Chemical Engineering Young, James; National Renewable Energy Laboratory Bedford, Nicholas M.; University of New South Wales; University of New South Wales; Colorado School of Mines, Department of Chemistry Miller, Elisa; National Renewable Energy Laboratory, Chemical and Nanoscience Thoi, V.; Johns Hopkins University, Department of Chemistry; Johns Hopkins University, Department of Materials Science and Engineering

Conformal Electrochemical Deposition of Intermetallic AuCu Thin Films for Convergent C-N Coupling

Carter S. Gerke[1†], Gregory D. Y. Foley[1†], Logan M. Wilder[3], Yuwei Yang[4,5], James L. Young[3], Nicholas M. Bedford[4,5,6], Elisa M. Miller[3], V. Sara Thoi[1,2]*

[†]These Authors Contributed Equally

[1] Department of Chemistry, Johns Hopkins University, Baltimore, Maryland 21218, USA.
[2] Department of Materials Science and Engineering, Johns Hopkins University, Baltimore, Maryland 21218, USA.
[3] Chemistry and Nanoscience Center, National Renewable Energy Laboratory, Golden, Colorado 80204, USA.
[4] School of Chemical Engineering, University of New South Wales, Syndey, New South Wales 2052, Australia.
[5]ARC Centre of Excellence in Carbon Science and Innovation, University of New South Wales 2052, Australia.
[6]Department of Chemistry, Colorado School of Mines, Golden, Colorado 80401, USA.

*corresponding author, email: sarathoi@jhu.edu

Abstract

Intermetallic AuCu alloys exhibited enhanced selectivity and activity for urea ($CO(NH_2)_2$) production compared to their parent metals. Intermetallic AuCu alloy thin films were grown electrochemically onto Ti foil substrates and were evaluated for their capacity to enable electrochemical C-N coupling. Varying the Au and Cu stoichiometry provided a synthetic handle to tune the film electronics (i.e., *d*-band position, oxophilicity) while maintaining overall film stability. The AuCu alloy with the highest Au loading of 75% proved to be the most electrochemically stable and possessed the highest selectivity (~68%) for urea formation. X-ray Absorption Spectroscopy (XAS) revealed that the Cu in alloys with more Au content maintained a higher oxidation state (in the form of Cu-O) under electrochemically relevant conditions. This observation suggests enhanced anion (NO_3^-/NO_2^-) adsorption and retention at the surface. This work highlights the utility of using intermetallic alloys to enable complex electrochemical coupling reactions by finely tuning material properties.

Introduction

Electrocatalysis provides a unique opportunity for utilizing renewably sourced electrical energy to generate essential value-added chemical feedstocks from thermodynamically spent "waste" compounds. Specifically, efforts in electrochemical carbon dioxide reduction reaction (CO_2RR) illustrate that CO_2, a common industrial waste product and greenhouse gas, can be transformed into useful industrial products.[1–5] The maturation of CO_2RR as a field has raised new opportunities to focus on furthering the synthetic complexity of CO_2 reduction with the introduction of new coupling partners. Prime examples of this include the electrochemical carboxylation of organic substrates[6], asymmetric cross coupling between different carbon-based precursors[7], and heteroatomic bond forming reactions (C-N, C-S, etc.).[8–11]

Electrochemical C-N bond formation is an appealing green method to produce industrially relevant organonitrogen compounds, like urea, formamide, and methylamine.[12–15] Urea is an essential industrial chemical currently generated on the order of 200 million tons annually and is used primarily as an agricultural fertilizer. Industrially, urea is prepared through the thermal conversion of ammonia, derived from the Haber-Bosch process, and carbon dioxide, which first forms ammonium carbamate, before resulting in the final product, urea. To drive this two-step reaction, high temperatures of up to 360 ºC and pressures of 150 bar are necessary.[16] Alternatively, nitrogen-containing reactants can be sourced from abundant feedstocks including NO_x compounds and reduced with CO_2 electrochemically to form C-N bonds.[17] However, as in CO_2RR, electrochemical C-N coupling often suffers from poor product selectivity, due to competition with the direct reduction of carbon and nitrogen reactants and the hydrogen evolution reaction (HER).[18]

Strategies within electrochemical CO_2RR literature can inspire new approaches to C-N bond formation. Many material design parameters have been evaluated for their effects on product distributions in CO_2RR including elemental composition[18], surface strain[19], *d*-band energetics[20], facet selection[21], and grain boundaries.[22] Intermetallic and bimetallic electrocatalysts are attractive design choices due to their tunable *d*-band electronics. In the modulation of metal stoichiometry, the electronic states of the material can be tuned to optimize the intermediate binding affinities to vary product selectivity and activity.[23,24] Within CO_2RR, a common strategy for C_{2+} product enhancement has been the incorporation of additional elements to well-established Cu-based catalysts. Specifically, various reported intermetallic and bimetallic catalyst systems have been used to enhance CO_2RR selectivity towards target products such as CH_4, C_2H_4, CO, and formate.[20,25–28] Within C-N coupling, bimetallic catalyst systems, such as Pd-Cu and Te-doped Pd nanomaterials, have effectively catalyzed electrochemical urea production, illustrating alloys have rich chemistry for exploration.[29,30]

In our previous work, we have shown that the electrochemical coupling between CO_2 and NO_3^- at polycrystalline gold electrodes can result in high selectivity (60.4% Faradaic efficiency) and activity (300 uA cm^{-2}) towards urea production.[31] The primary limitations of this earlier system were the inhibitory cost of the precious metal electrode and the high Faradaic losses to other nitrate reduction reaction (NO_3RR) products, including nitrite (NO_2^-) and ammonia (NH_3). In addition, a previous report developed AuCu nanofibers active for urea production from CO_2 and NO_2^-.[32] Nevertheless, the role of Au to Cu stoichiometry on electronic effects within intermetallic catalysts

remains underexplored within C-N coupling reactions. Herein, we selected AuCu intermetallic alloys as a platform to explore the impacts of electronic effects on C-N coupling. Importantly, AuCu-based alloys have been previously used for electrochemical CO_2RR with varying product selectivity due to differences in catalyst design.[25,27,28] Moreover, electronic effects were found to be an essential factor in determining reactivity of AuCu thin films.[20] In our work, we found that varying the Au:Cu molar ratio enabled us to tune adsorbate interactions while also maintaining film integrity. Using X-ray photoelectron spectroscopy and *in situ* X-ray absorption spectroscopy, we attributed the increased Faradaic efficiency (up to 68%) and activity (on the order of 350 μA cm^{-2}) for urea to the diversion of the previously espoused $*NO_2$ intermediate away from deleterious side products including NO_2^- and NH_3 in favor of C-N coupling towards urea. Our work adds new knowledge to the growing field of electrochemical C-N coupling.

Experimental Section

Synthesis of Intermetallic Au_xCu_{100-x} Alloy Electrodes.

Ti electrodes (2x1 cm^2) were cut from a polycrystalline Ti foil (0.25 mm thick, Sigma, 99.7%) and prepared by polishing with Si-C (600 grit) paper, sonicating in dilute nitric acid (5% in water) and then in water three times. Electrical contact was accomplished by wrapping with Ti wire. In a plating solution consisting of tetrahydrofuran (THF), ethanol (EtOH), sulfuric acid (H_2SO_4), and water (H_2O) (in the ratios of 30, 15, 10, and 45 vol%), aliquots of concentrated, aqueous, gold trichloride ($AuCl_3$) and copper sulfate ($Cu(SO_4)_2$) salt solutions were added in various molar quantities to bring the total metal (Au + Cu) salt concentration to 20 mM. The optimal ratios to prepare alloys with approximate stoichiometries of Au_xCu_{100-x} with x = 75, 50 and 25 were achieved with deposition solutions containing 85, 65, and 27.5 mol% Au, respectively. Electroplating occurred at -0.25 V vs. Ag/AgCl for 30 min, with the working electrode being removed from the bath solution just before the potential was shut off to avoid galvanic exchange of the residual Au(III) in solution with surface Cu(0). The synthesized electrodes were then washed extensively with water and dried under an N_2 stream. Freshly prepared electrode surfaces were characterized by scanning electron microscopy (SEM), energy dispersive X-ray spectroscopy (EDS), X-ray Photoelectron Spectroscopy (XPS), Grazing Incidence X-ray Diffraction (GIXRD), and cyclic voltammetry (CV).

Electrochemical Experiments.

Controlled-potential electrolysis experiments were carried out on a CHI660 potentiostat in a commercial liquid flow cell from DEK International. The nitrate (KNO_3, 0.1 M) electrolyte was prepared by dissolving trace-metal grade salts in high purity water (>18.2 MΩ cm). Electrolyte was then purged with either N_2 or CO_2 gas, when purged with CO2 the 0.1 M KNO_3 solution reached a stable pH of 3.5. Electrolyte was used within two days of preparation. The anodic and cathodic compartments were separated by a Nafion 115 membrane. Each compartment was connected in parallel to a catholyte and anolyte compartment that was charged with 15 mL of electrolyte with 35 mL remaining in the headspace. Nickel foam served as the counter electrode and was placed in the anodic compartment of the flow cell. The reference electrode used in this study was an eDAQ leakless Ag/AgCl electrode and was placed in the cathodic compartment level to the working electrode. Both electrolyte reservoirs were purged with CO_2 gas for 15 min prior to

each electrolysis experiment. During each experiment, the cathodic compartment was continuously purged at a rate ranging between 20-30 sccm. Prior to electrolysis the ohmic drop between the working and reference electrode was determined using potentiostatic electrochemical impedance spectroscopy (PEIS) at -0.2 V vs. RHE. Prior to all electrolysis experiments, the ohmic resistance is corrected at 100% iR compensation and the ohmic drop from the intermetallic electrodes was consistently between 20-30 Ω.

Results and Discussion

The primary interest of this work was to evaluate which material design parameters engender a higher degree of control over C-N coupling selectivity. To that end, we designed a system that would minimize contributions from mass transport limitations, including diffusional gradients of substrate and large pH swings at the interface, to specifically focus on the role the intermetallic system plays in the co-activation of CO_2 and NO_3^-. Therefore, conformally grown AuCu thin film were deposited on a Ti foil support by adapting a previously established method for preparing mesoporous Au_xCu_{100-x} electrodeposits.[33] The electroplating bath consisted of an acidic aqueous/ organic composite electrolyte (H_2O, THF, EtOH, H_2SO_4) heated to 50 °C. Due to the difference in the onset reduction potential between Cu and Au ions (**Figure 1a**), we surveyed a range of starting concentrations to achieve a wide distribution of alloy stoichiometries at the plating potential of -0.25 V vs. Ag/AgCl. The surface morphology of the synthesized films was then characterized by scanning electron microscopy (SEM), which depicted conformal growth across the Ti foil substrate (**Figure 1b, Figure S1**). With molar Au to Cu ratios of 85:15, 65:35, and 27.5:72.5 in the plating solutions, we achieved approximate Au to Cu stoichiometries of $Au_{75}Cu_{25}$, $Au_{50}Cu_{50}$, and $Au_{25}Cu_{75}$, respectively, as determined by energy dispersive X-ray spectroscopy (EDS) analysis (**Figure 1c**).

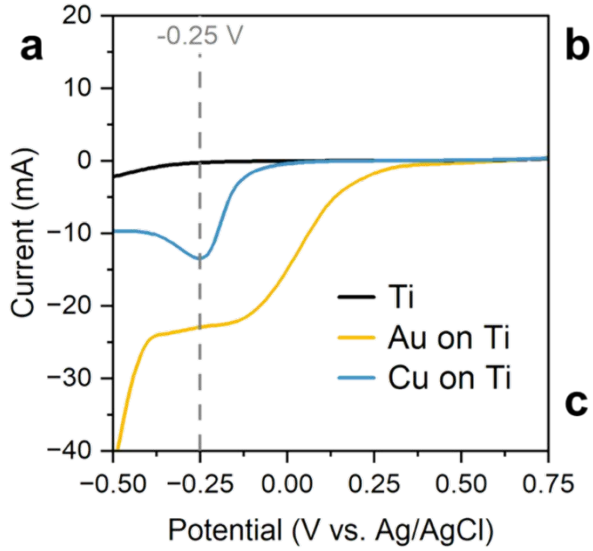

Sample Identity	Mol % Au in plating bath	Atom % Au by EDS	Atom % Cu by EDS
$Au_{75}Cu_{25}$	85	75.98	24.02
$Au_{50}Cu_{50}$	65	52.42	47.58
$Au_{25}Cu_{75}$	27.5	28.4	71.60

Figure 1. Electrochemical Deposition of Au and Cu ions onto a titanium foil substrate. (a) Linear sweep voltammograms of a fresh Ti electrode in the plating bath held at 50 °C in the absence (black) and presence of either 10 mM Au (yellow) or Cu (blue) salts (100 mV s^{-1}). The dotted vertical line indicates the potential chosen (-0.25 V vs. Ag/AgCl) for the co-deposition of Au and

Cu. (b) Representative SEM images of the Ti foil electrode and three freshly prepared AuCu alloys (the scale bar represents 20 μm in each image). (c) Tabulated values of bulk film composition following electrodeposition as determined by EDS.

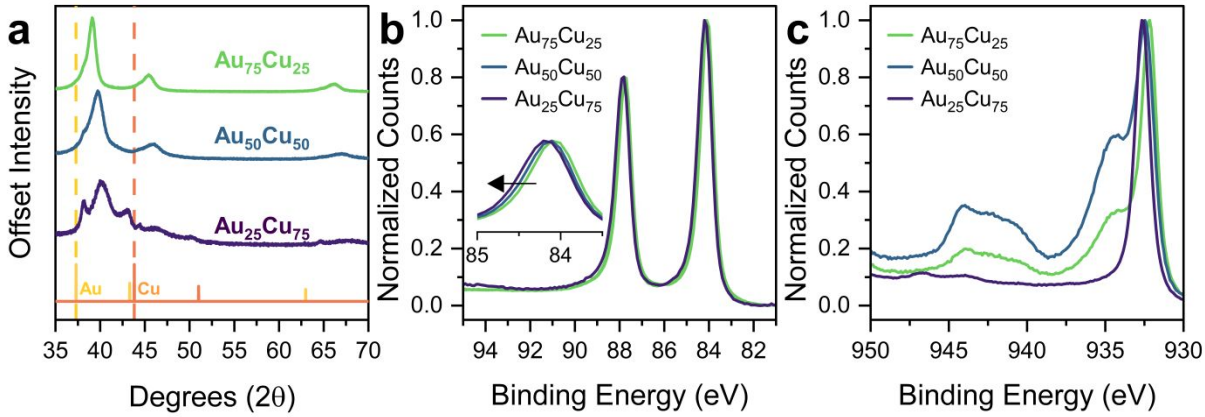

Figure 2. X-ray Characterization of AuCu films. (a) Grazing incidence X-ray Diffraction Spectroscopy (GIXRD) of the intermetallic alloys collected at a 0.4° angle offset. X-ray Photoelectron Spectroscopy (XPS) of the (b) Au 4*f* with inset showing a progression to higher binding energies with increasing copper content and (c) Cu 2*p* regions.

The crystalline phase purity of the alloy films was determined through grazing incidence X-ray diffraction (GIXRD) using an optimal angle offset of 0.4° (**Figure S2**). The GIXRD results showed pure intermetallic alloy phases for the $Au_{75}Cu_{25}$ and $Au_{50}Cu_{50}$ composite electrodes with a peak shift consistent with Vegard's law, as the lattice parameter is reduced with increasing copper stoichiometry (**Figure 2a**). The phase purity is lost in the $Au_{25}Cu_{75}$ electrode as three distinct diffraction peaks are present for the (111) index representing Au-rich, Cu-rich, and an intermetallic phase. However, the primary reflection of the alloy still follows the trend of the two higher Au-containing intermetallic samples. In addition, our GIXRD data is consistent with the characterization within previous report of AuCu alloy intermetallic on titanium foils substrates.[20]

The alloy films were further characterized with X-ray Photoelectron Spectroscopy (XPS) to determine the surface composition (top ~10 nm) of the AuCu alloys (**Figure 2b,c**). We observe a higher Cu to Au atomic ratio at the surface than expected from the EDS measurements. This higher Cu concentration is likely due to the presence of surface oxides that are expected to form on low coordinate Cu at the surface upon ambient air exposure. The copper oxides have distinctive satellite features that can be clearly observed in **Figure 2c**: satellite peaks corresponding to CuO (940 – 945 eV) for $Au_{75}Cu_{25}$ and $Au_{50}Cu_{50}$ and Cu_2O (943 – 947 eV) for $Au_{25}Cu_{75}$, respectively. We note that during electrocatalysis, these surface oxides are largely reduced to metallic Cu as reported in previous literature.[34] Indeed, the XPS spectrum of $Au_{75}Cu_{25}$ after electrolysis showed a decrease in the Cu to Au atomic ratios, with values that are closer to those of the bulk stoichiometry found in the initial EDX measurements (**Figure S3-4, Table S1-2**). Furthermore, we note that rather than shifting towards lower binding energies, the Au 4*f* feature shifts to higher binding energies with increasing Cu to Au ratio (**Figure 2b**).[35] This is another indication of the

presence of surface oxides on the Cu atoms that vary between the three alloys; as the surface oxides could influence the energetic/dipole at the surface of the films, which would result in a shift toward higher binding energies for the Au *4f* peak. (**Figure 2c**).

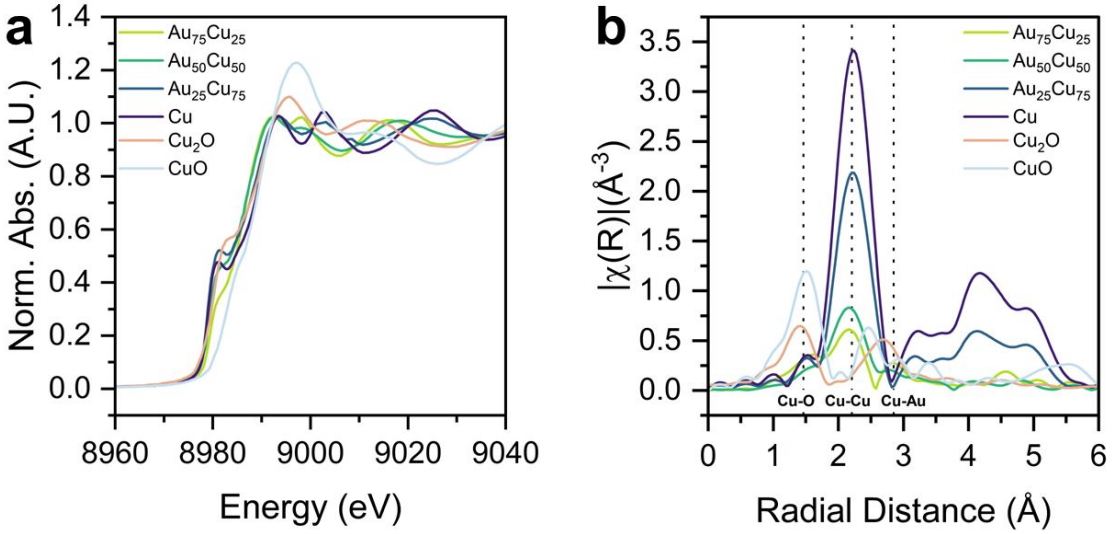

Figure 3. *Ex situ* X-ray Absorption Spectroscopy. Cu K-Edge (a) X-ray Absorption Near Edge Structure (XANES) and (b) Extended X-ray Absorption Fine Structure (EXAFS) spectra of AuCu alloys and relevant copper and copper oxide controls.

To analyze the electronic structure and local coordination environment of the three alloys, we use X-ray absorption spectroscopy (XAS) of the Cu K- and Au L_3-edges. *Ex situ* XAS characterization displayed more distinct trends for the Cu K-edge than for the Au L_3-edge of each alloy **(Figure 3, Figure S5).** In the X-ray absorption near edge structure (XANES) of the Cu K-edge, we observe an increase in edge energy with increasing Au content, indicating a decrease in the electron density of Cu within the bulk materials **(Figure S6)**.[35] Furthermore, the rising edge feature and post-edge profile of $Au_{50}Cu_{50}$ and $Au_{75}Cu_{25}$ spectra display distinct features that reflect the different coordination environments in the intermetallic alloy (**Figure 3a**).[36] In contrast, the $Au_{25}Cu_{75}$ spectrum matches most closely with that of a metallic Cu standard, confirming the presence of Cu-rich phases. Additionally, the XANES profile, edge energies (E_0), and the white line intensities of each alloy more closely resemble those parameters of metallic Cu rather than those of Cu_2O and CuO **(Figure 3a).** The distinction from Cu_2O and CuO and likeness to metallic Cu is made more apparent by derivative normalized energy plots of the XANES (**Figure S6b**). Post-edge features are structure-sensitive components of the XANES spectra and are influenced greatly by the local coordination environment, interatomic distances, and particle sizes.[35,37–40]For example, both the $Au_{50}Cu_{50}$ and $Au_{75}Cu_{25}$ spectra contain a post-edge feature at about 9000 eV, corresponding to higher oxidation state Cu **(Figure 3a)**.[36] Moreover, the post-edge features trend to lower energies with increasing Au content, which is attributed to the lattice expansion of Cu.[36,41]For the Au L_3-edge, we observe the expected reverse trend; the post-edge region features trend towards slightly higher energies with increasing Cu content, corresponding to the lattice compression of Au (**Figure S5a**).[36,41]

We further explored the local coordination environment of the alloys with extended X-ray absorption fine structure (EXAFS). All k–space fittings along with EXAFS modeling results can be found in the supporting information (**Figures S7-12, Tables S3-S5**). The EXAFS data confirms the lattice expansion and compression of Cu and Au, respectively. The Cu-Cu bond distances (2.54 ± 0.01, 2.56 ± 0.00, and 2.64 ± 0.02 Å, respectively) in $Au_{25}Cu_{75}$, $Au_{50}Cu_{50}$, and $Au_{75}Cu_{25}$ shift to larger values with increasing Au content, indicating Cu lattice expansion. For the Cu K-edge, the EXAFS data also distinguishes the $Au_{25}Cu_{75}$ material with more metallic copper character, as higher atomic order is observed with 3rd and 4th shell scattering features (within the 4 – 6 Å region) matching with features of the copper standard (**Figure 3b**).[42] Moreover, both the $Au_{50}Cu_{50}$ and $Au_{75}Cu_{25}$ alloys display a clear Cu-Au scattering feature, while $Au_{25}Cu_{75}$ does not (**Figure 3b, S6c**). Therefore, our *ex situ* XAS analysis suggests that Cu oxidation state increases with Au content and $Au_{25}Cu_{75}$ possesses some bimetallic character compared to the intermetallic character of both $Au_{50}Cu_{50}$ and $Au_{75}Cu_{25}$, consistent with our characterization of copper-rich phases in the $Au_{25}Cu_{75}$ alloy by GIXRD. In addition, as the Cu K-edge EXAFS data lacks features of Cu_2O and CuO, the intermetallic alloys do not contain copper oxide in the bulk (**Figure 3b**). Furthermore, the wavelet transformation plots of the *ex situ* Cu K-edge of the AuCu films more closely resemble the plot of metallic Cu than those of Cu_2O, and CuO standards (**Figure S13**). Additionally, the $Au_{75}Cu_{25}$ and $Au_{50}Cu_{50}$ wavelets contain a relatively intense feature corresponding to Cu-Au coordination (8, 2.25), further confirming their intermetallic character, with a less intense Cu-O feature. The plot of $Au_{25}Cu_{75}$ mostly resembles that of metallic Cu, which again suggests the presence of Cu-rich domains.

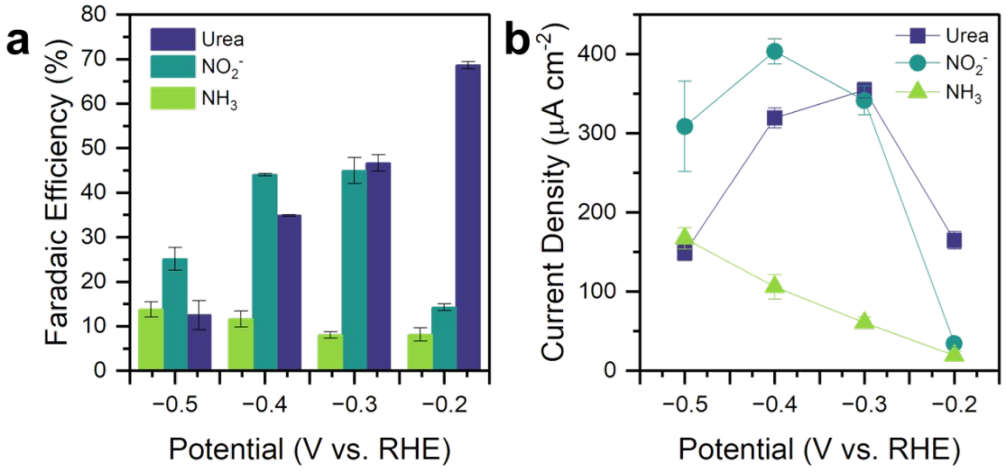

Figure 4. Electrochemical Performance of the $Au_{75}Cu_{25}$ Electrode Material. (a,b) Chronoamperometry results for the $Au_{75}Cu_{25}$ alloy between -0.2 and -0.5 V vs. RHE for 1 h in a continuously CO_2 purged solution of 0.1 M KNO_3, pH 3.5.

The electrochemical activity for the AuCu alloy catalysts were next evaluated for the convergent reduction of CO_2 and NO_3^- to generate urea. Electrocatalysis experiments were performed in an electrochemical liquid flow cell using 0.1 M KNO_3, under continuous CO_2 purging, maintaining a

pH of 3.5. A series of galvanostatic electrolysis experiments were used to survey the $Au_{75}Cu_{25}$, $Au_{50}Cu_{50}$, and $Au_{25}Cu_{75}$ alloys and their parent metals under both C-N coupling conditions and isolated CO_2RR or NO_3RR control conditions. At the applied current densities of -0.25, -0.5, and -1.0 mA cm^{-2}, all the alloys outperformed both pure Au and Cu catalysts in selectivity for urea production (**Figure S14-S15**). Control CO_2RR and NO_3RR experiments were conducted using Au, Cu, and the three alloy composite electrodes (**Figure S16**). In the CO_2RR control experiments, it was observed that the $Au_{75}Cu_{25}$ alloy behaved the most like the parent Au electrode with a high selectivity for CO, while CO selectivity was reduced in favor of H_2 evolution with increasing Cu incorporation. In the NO_3RR control conditions, it was found that NO_2^- was the only major product across all electrode materials. We speculate CO_2 plays a critical role in maintaining a low electrolyte pH necessary for generating further reduced nitrogen-containing products (i.e. urea and ammonia).[43]

We next evaluated the stability of the alloys following electrochemical C-N coupling. The $Au_{75}Cu_{25}$ alloy maintained its morphology and stoichiometry by SEM and EDS when electrolyzed at -0.5 mA cm^{-2}, whereas $Au_{25}Cu_{75}$ alloy displayed significant corrosion at the same current density (**Figure S17)**. The films generally remained intact at lower cathodic potentials **(Figure S18**). As the highest selectivity and activity metrics for urea was achieved with the $Au_{75}Cu_{25}$ electrode, the potential-dependent performance of $Au_{75}Cu_{25}$ was further explored. Controlled potential electrolysis was conducted for 1 hour at four potentials: -0.2, -0.3, -0.4, and -0.5 V vs. RHE (**Figure 4**). An optimal Faradaic efficiency of 68.6 ± 0.8% was obtained at -0.2 V with a current density of 164 ± 11 μA cm^{-2}. A peak current density of 354.4 ± 9.9 μA cm^{-2} was achieved at -0.3 V with a Faradaic efficiency of 46.6 ± 1.8%. Extended electrolysis using the $Au_{75}Cu_{25}$ catalyst at -0.3 V vs RHE displays only a marginal difference in urea selectivity over three hours (**Figure S19**). Urea and nitrite selectivity were found to increase and decrease together within our potential range, suggesting that their production follows similar yet competing reaction pathways. Ammonia did not follow this trend; rather its activity scaled with increasing cathodic potentials (**Figure 4b**). Electrokinetic analysis showed a rate order dependence of nitrate concentration on the various observed products. Nitrite production showed a near first-order dependence on nitrate (x = 0.8), while ammonia production showed a zeroth-order dependence (x = -0.01) (**Figure S21**). These trends support a mechanism featuring an early-stage reduction intermediate for C-N coupling

The above finding is in agreement with previous computational pathways for urea production from NO_3^- and CO_2.[31,44,45] In general, nitrate electroreduction to ammonia over polycrystalline metal and alloy composite materials follows either a PCET of associatively adsorbed *NO or dissociative adsorption of nitric oxide followed by hydrogenation of *N adsorbates by *H.[46–49] In our previous report on a polycrystalline Au electrode, we found the lowest energetic pathway for urea synthesis from CO_2 and NO_3^- to occur via the coupling of early stage reduction intermediates (*CO_2 and *NO_2 → *NO_2CO_2), effectively bifurcating selectivity of the NO_3RR pathways away from surface *NO species and deselecting for ammonia production. The operative intuition behind this work was to enhance the formation and stability of the *NO_2 intermediate by synthesizing gold alloys with varying concentrations of Cu, which is commonly attributed to having enhanced interactions with adsorbates. Indeed, electrolysis under similar conditions at -0.2 V vs. RHE showed a ~5-fold increase in urea selectivity balanced with a ~4-fold decrease in nitrite selectivity for the AuCu

alloy compared results of the polycrystalline Au. The high selectivity for urea is limited to a small potential window due to competing *NO_2 reduction to NO_2^- (-0.3 to -0.4 V vs. RHE) and *H formation (-0.4 V vs. RHE). While we cannot spectroscopically resolve *H adsorbates, *in situ* Raman spectroscopy supports our electrochemical results: the NO_2^- bands increased between the potentials of -0.2 to -0.4 V but disappeared at -0.5 V where H* adsorbates outcompete NO_2^- binding and conversion (**Figure S20**). We speculate that the increased selectivity for urea at low applied potentials corresponds with the incorporation of Cu sites that favors the binding of nitrate reduction intermediates.

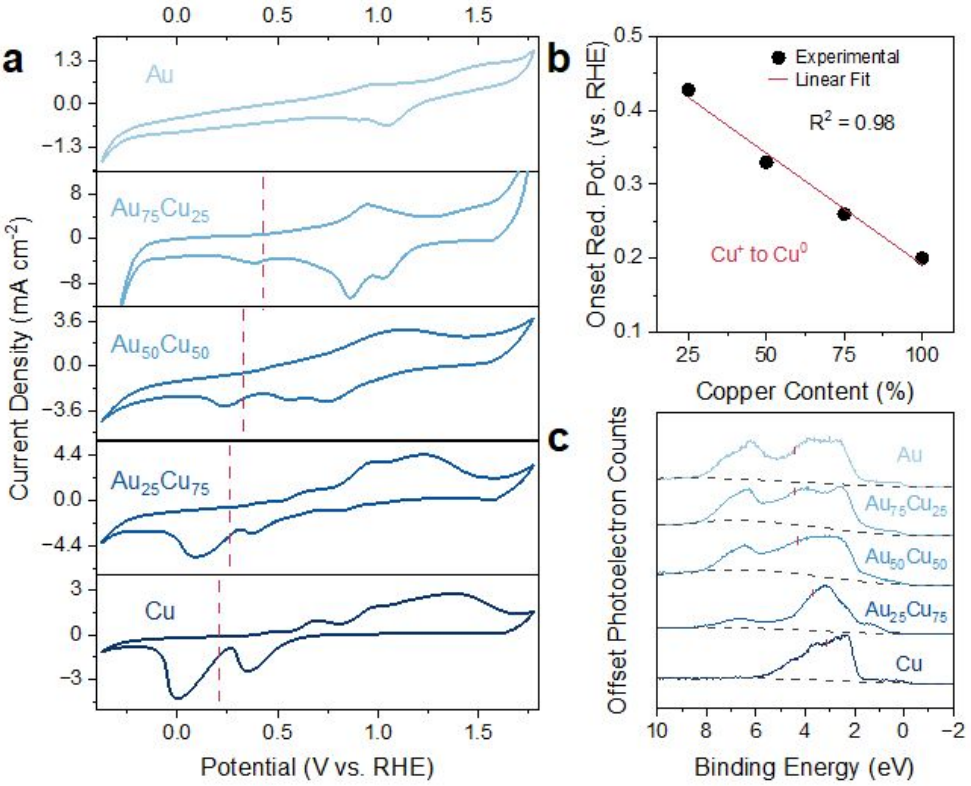

Figure 5. Using Cyclic Voltammetry and *d*-band Energetics. (a) Cyclic Voltammetry (CV) of (top to bottom) Au, $Au_{75}Cu_{25}$, $Au_{50}Cu_{50}$, $Au_{25}Cu_{75}$, and Cu in 0.5 M KOH at 100 mV/s, red lines denote the $Cu^{1+/0}$ onset potentials. (b) The linear relationship between Cu content and the onset reduction potential of the three Au:Cu alloys and a Cu electrode defined as the peak relating to the Cu^+ to Cu^0 reduction feature (red dashes in Figure 5a). (c) The valence band structure obtained by X-ray photoelectron spectroscopy representing a shift in the *d*-band center, towards the Fermi level, with increasing Cu content.

Previous work has established that the oxygen binding energy of a material is correlated to its standard reduction potential (**Figure S22**).[26] Therefore, cyclic voltammetry can be utilized to characterize the apparent oxophilicity of the AuCu alloy systems as it pertains to the binding strength of our proposed, O,O bound intermediate, *NO_2. We find that anodic CVs show characteristic oxidation and reduction features consistent with the parent metals with similar

features appearing for the three alloy systems. Owing to the poor distinction between the AuO_x and $Cu^{2+/1+}$ reduction waves, we elected to characterize the $Cu^{1+/0}$ redox feature (**Figure 5a**). Interestingly, we found that this reduction feature scales linearly with the bulk Cu content (**Figure 5b**); oxidation of Cu^+ is more favorable with higher Cu stoichiometries. We speculate that the higher oxophilicity of AuCu alloys compared to metallic Au likely promotes the binding of NO_3RR intermediates, specifically $*NO_2$, during catalysis. To further support this assertion, we collected the valance band structure via XPS, which displays a progression of the *d*-band center towards the Fermi level with increasing Cu content (**Figure 5c**). This observation follows the previously espoused *d*-band theory, which relates the strength of the bond formation between adsorbate ($*NO_2$) molecular orbitals and transition metal *s* and *d* states to the position of the *d*-band center.[20,50]

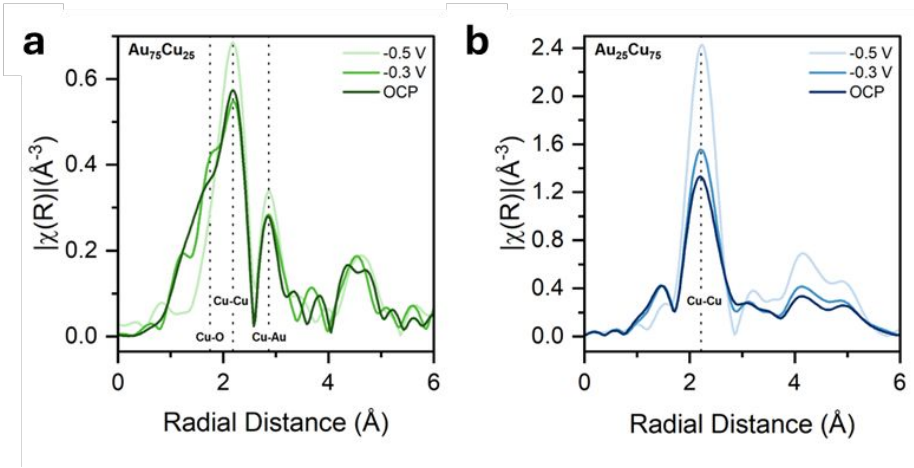

Figure 6. *In situ* Cu K-Edge EXAFS of the $Au_{25}Cu_{75}$ and $Au_{75}Cu_{25}$. EXAFS spectra for the (a) $Au_{75}Cu_{25}$ and (b) $Au_{25}Cu_{75}$ alloy electrodes under a potential bias of OCP, -0.3 V, and -0.5 V vs. RHE in a pH 3.5 solution of 0.1 M KNO_3, pH 3.5, under flowing CO_2 conditions.

To describe changes in the electronic structure and coordination environment of each AuCu alloy catalyst, *in situ* X-ray absorption spectroscopy (XAS) was conducted under experimentally relevant conditions: open-circuit potential (OCP), the catalytically optimized potential of –0.3 V vs. RHE, and –0.5 V vs. RHE. Only slight changes were observed in the *in situ* Cu K-edge XANES spectra of $Au_{50}Cu_{50}$ and $Au_{75}Cu_{25}$ from OCP to -0.3 V (**Figure S23**).[35,51] Notably, an applied potential of –0.5 V vs. RHE alters the Cu XANES post-edge region of the $Au_{75}Cu_{25}$ alloy distinctly, indicating a change in coordination environment that may correspond to surface reduction of copper oxides.[36] This observation is consistent with our electrochemical data: the selectivity and activity for urea significantly decreases at -0.5 V (**Figure 4**). In contrast, the $Au_{25}Cu_{75}$ alloy features a decrease in the rising absorption edge intensity (white-line) and resembles the profile of the *ex situ* spectra at –0.5 V vs. RHE (**Figure 3a**), indicating a decrease in Cu valence and a return to metallic Cu character (**Figure S23**).[35,51] Notably, no significant changes within the Au L_3-edge *in situ* XANES spectra were observed for all three AuCu alloys (**Figure S24**).

The *in situ* Cu K-edge EXAFS modeling revealed distinct changes in the coordination environment of the alloys during electrolysis (**Figure 6, Figure S25 & S26**). The Cu K-edge fitting of $Au_{75}Cu_{25}$

displays a Cu-Cu coordination decrease from OCP (1.05 ± 0.41) to –0.3 V vs. RHE (0.89 ± 0.44) and subsequent increase to –0.5 V vs. RHE (1.95 ± 0.23) (**Figure 6a, Table S3, Figure S27a**). We observe a retention of Cu-O coordination from OCP to –0.3 V vs. RHE for $Au_{75}Cu_{25}$, with coordination numbers of 0.83 ± 0.13 and 0.95 ± 0.21, respectively (**Table S3, Figure S27b**). Moreover, the Cu K-edge fitting of $Au_{75}Cu_{25}$ displays a prominent Cu-O feature at –0.3 V vs. RHE (**Figure 6a**).[52,53] The retention of Cu-O coordination and prominent Cu-O feature at -0.3 V vs. RHE even under a cathodic bias may indicate adsorption of reaction intermediates **(Figure 6a, Figure S27 & 28).**[12,35,53] Similar coordination number trends were observed for $Au_{50}Cu_{50}$, notably the retention of Cu-O (**Table S4**).

In contrast, the Cu K-edge fitting of $Au_{25}Cu_{75}$ shows that the 3rd and 4th shell scattering features (within the 4–6 Å region) become more pronounced with more cathodic applied potentials, indicating higher atomic order in Cu-Cu coordination approaching that of metallic Cu (**Figure 6b, Figure S27**).[42] In addition, the Cu-Cu scattering intensity of the $Au_{25}Cu_{75}$ alloy increases with increased cathodic bias; Cu-Cu coordination increases significantly from 5.16 ± 0.43 at -0.3 V to 7.96 ± 0.31 at -0.5 V vs. RHE (**Figure 6b, Table S5, Figure S27a**). We also observe a decrease in Cu-O coordination with increased cathodic bias, with a coordination number of nearly 0 at -0.5 V vs. RHE, corresponding to a decrease in Cu valence (**Table S5, Figure S27a**).[52,53] The significant increase in Cu-Cu coordination number for $Au_{25}Cu_{75}$ alloy and the return to metallic Cu character with increasing cathodic potential suggest a loss of intermetallic character.[12,35,36,51,53] The overall Cu coordination in the $Au_{25}Cu_{75}$ alloy is reduced with changes in potential and subsequently increases at –0.5 V vs. RHE. These features may indicate Cu leaching as a function of potential, with a loss of intermetallic character into metallic Cu at –0.5 V vs. RHE. We note that each alloy is likely surface-enriched with Cu since the total coordination number of Cu is lower than that of Au, which is in accordance with our XPS findings (**Figure S29**, **Table S3-S5**). Overall, the *in situ* XAS characterization consistently supports enhanced electrochemical stability under C-N coupling conditions of $Au_{75}Cu_{25}$ and $Au_{50}Cu_{50}$ compared to that of $Au_{25}Cu_{75}$.

Conclusion

In this work, intermetallic AuCu thin films were prepared to investigate how material design parameters impact electrochemical C-N bond formation. Through extensive material and electrochemical characterization, we reveal a correlation between Au:Cu stoichiometry, catalyst-adsorbate binding, and C-N selectivity. With electrochemical optimization, we found the alloy with the highest Au loading ($Au_{75}Cu_{25}$) to be the most selective (~68%) and active (~355 μA cm^{-2}) for urea production. Moreover, higher Au content was found to positively correlate with film stability under cathodic polarization. *In situ* X-ray absorption spectroscopy under experimentally relevant conditions corroborated our observations, revealing that higher Au incorporation within the alloy catalysts maintained intermetallic character and Cu in a higher oxidation state. In addition, the Cu-O coordination number increased at catalytically relevant potentials, which suggests enhanced adsorption of potential *NO_2 reaction intermediates. Our findings highlight how the tunable nature of alloy materials can be leveraged to facilitate complex electrochemical reactions such as C-N bond formation.

Acknowledgments

C.S.G., G.D.Y.F., and V.S.T. acknowledge support from the U.S. Department of Energy (DOE), Office of Science, Office of Basic Energy Sciences, Catalysis Science program, under Award DE-SC0021955. C.S.G acknowledges the U.S. Department of Energy (DOE) Office of Science Graduate Student Research (SCGSR) program for funding. The SCGSR program is administered by the Oak Ridge Institute for Science and Education (ORISE) for the DOE under contract number DE-SC0014664. C.S.G. would also like to acknowledge the National Science Foundation Graduate Research Fellowship Program (DGE1746891). N.M.B and Y.Y. acknowledge funding from the Australian Research Council Centre of Excellence in Carbon Science and Innovation (ARC CoE-CSI) (CE230100032). Portions of this research were carried out at National Synchrotron Light Source II (beamline 6-BM) with the assistance of Dr. Bruce Ravel, a U.S. Department of Energy (DOE) Office of Science User Facility operated for the DOE Office of Science by Brookhaven National Laboratory under Contract No. DE-SC0012704. This work was authored, in part, by the National Renewable Energy Laboratory (NREL), operated by the Alliance for Sustainable Energy, LLC, for the US Department of Energy (DOE) under contract no. DE-AC36-08GO28308. The work at NREL was supported by the Solar Photochemistry Program, Division of Chemical Sciences, Geosciences, and Biosciences, Office of Basic Energy Sciences, US DOE. This funding supported electrochemical studies with product detection as well as the XPS studies. J.L.Y acknowledges support from the Cleantech project funded by the U.S. Department of Energy, Office of Science, Basic Energy Science. The views expressed in the article do not necessarily represent the views of the DOE or the U.S. Government. The U.S. Government retains and the publisher, by accepting the article for publication, acknowledges that the U.S. Government retains a nonexclusive, paid-up, irrevocable, worldwide license to publish or reproduce the published form of this work, or allow others to do so, for U.S. Government purposes.

References

(1) Saha, P.; Amanullah, S.; Dey, A. Selectivity in Electrochemical CO_2 Reduction. *Acc. Chem. Res.* **2022**, *55* (2), 134–144. https://doi.org/10.1021/acs.accounts.1c00678.

(2) Rossi, K.; Buonsanti, R. Shaping Copper Nanocatalysts to Steer Selectivity in the Electrochemical CO_2 Reduction Reaction. *Acc. Chem. Res.* **2022**, *55* (5), 629–637. https://doi.org/10.1021/acs.accounts.1c00673.

(3) Overa, S.; Ko, B. H.; Zhao, Y.; Jiao, F. Electrochemical Approaches for CO_2 Conversion to Chemicals: A Journey toward Practical Applications. *Acc. Chem. Res.* **2022**, *55* (5), 638–648. https://doi.org/10.1021/acs.accounts.1c00674.

(4) Banerjee, S.; Gerke, C. S.; Thoi, V. S. Guiding CO_2RR Selectivity by Compositional Tuning in the Electrochemical Double Layer. *Acc. Chem. Res.* **2022**, *55* (4), 504–515. https://doi.org/10.1021/acs.accounts.1c00680.

(5) Cohen, K. Y.; Evans, R.; Dulovic, S.; Bocarsly, A. B. Using Light and Electrons to Bend Carbon Dioxide: Developing and Understanding Catalysts for CO_2 Conversion to Fuels and Feedstocks. *Acc. Chem. Res.* **2022**, *55* (7), 944–954. https://doi.org/10.1021/acs.accounts.1c00643.

(6) Yang, D.-T.; Zhu, M.; Schiffer, Z. J.; Williams, K.; Song, X.; Liu, X.; Manthiram, K. Direct Electrochemical Carboxylation of Benzylic C–N Bonds with Carbon Dioxide. *ACS Catal.* **2019**, *9* (5), 4699–4705. https://doi.org/10.1021/acscatal.9b00818.

(7) Chen, C.; Yu, S.; Yang, Y.; Louisia, S.; Roh, I.; Jin, J.; Chen, S.; Chen, P.-C.; Shan, Y.; Yang, P. Exploration of the Bio-Analogous Asymmetric C–C Coupling Mechanism in Tandem CO2 Electroreduction. *Nat Catal* **2022**, *5* (10), 878–887. https://doi.org/10.1038/s41929-022-00844-w.

(8) Tao, Z.; Rooney, C. L.; Liang, Y.; Wang, H. Accessing Organonitrogen Compounds via C–N Coupling in Electrocatalytic CO_2 Reduction. *J. Am. Chem. Soc.* **2021**, *143* (47), 19630–19642. https://doi.org/10.1021/jacs.1c10714.

(9) Rooney, C. L.; Wu, Y.; Tao, Z.; Wang, H. Electrochemical Reductive N-Methylation with CO_2 Enabled by a Molecular Catalyst. *J. Am. Chem. Soc.* **2021**, *143* (47), 19983–19991. https://doi.org/10.1021/jacs.1c10863.

(10) Li, J.; Zhang, Y.; Kuruvinashetti, K.; Kornienko, N. Construction of C–N Bonds from Small-Molecule Precursors through Heterogeneous Electrocatalysis. *Nat Rev Chem* **2022**, *6* (5), 303–319. https://doi.org/10.1038/s41570-022-00379-5.

(11) Gerke, C. S.; Xu, Y.; Yang, Y.; Foley, G. D.; Zhang, B.; Shi, E.; Bedford, N. M.; Che, F.; Thoi, V. S. Electrochemical C–N Bond Formation within Boron Imidazolate Cages Featuring Single Copper Sites. *J. Am. Chem. Soc.* **2023**, *145* (48), 26144–26151. https://doi.org/10.1021/jacs.3c08359.

(12) Friebel, D.; Viswanathan, V.; Miller, D. J.; Anniyev, T.; Ogasawara, H.; Larsen, A. H.; O'Grady, C. P.; Nørskov, J. K.; Nilsson, A. Balance of Nanostructure and Bimetallic Interactions in Pt Model Fuel Cell Catalysts: In Situ XAS and DFT Study. *J. Am. Chem. Soc.* **2012**, *134* (23), 9664–9671. https://doi.org/10.1021/ja3003765.

(13) Li, J.; Kornienko, N. Electrochemically Driven C–N Bond Formation from CO_2 and Ammonia at the Triple-Phase Boundary. *Chem. Sci.* **2022**, *13* (14), 3957–3964. https://doi.org/10.1039/d1sc06590d.

(14) Wu, Y.; Jiang, Z.; Lin, Z.; Liang, Y.; Wang, H. Direct Electrosynthesis of Methylamine from Carbon Dioxide and Nitrate. *Nat Sustain* **2021**, *4* (8), 725–730. https://doi.org/10.1038/s41893-021-00705-7.

(15) Tao, Z.; Wu, Y.; Wu, Z.; Shang, B.; Rooney, C.; Wang, H. Cascade Electrocatalytic Reduction of Carbon Dioxide and Nitrate to Ethylamine. *Journal of Energy Chemistry* **2022**, *65*, 367–370. https://doi.org/10.1016/j.jechem.2021.06.007.

(16) Yildirim, Ö.; Nölker, K.; Büker, K.; Kleinschmidt, R. Chemical Conversion of Steel Mill Gases to Urea: An Analysis of Plant Capacity. *Chemie Ingenieur Technik* **2018**, *90* (10), 1529–1535. https://doi.org/10.1002/cite.201800019.

(17) Liu, H.; Park, J.; Chen, Y.; Qiu, Y.; Cheng, Y.; Srivastava, K.; Gu, S.; Shanks, B. H.; Roling, L. T.; Li, W. Electrocatalytic Nitrate Reduction on Oxide-Derived Silver with Tunable Selectivity to Nitrite and Ammonia. *ACS Catal.* **2021**, *11* (14), 8431–8442. https://doi.org/10.1021/acscatal.1c01525.

(18) Nitopi, S.; Bertheussen, E.; Scott, S. B.; Liu, X.; Engstfeld, A. K.; Horch, S.; Seger, B.; Stephens, I. E. L.; Chan, K.; Hahn, C.; Nørskov, J. K.; Jaramillo, T. F.; Chorkendorff, I. Progress and Perspectives of Electrochemical CO_2 Reduction on Copper in Aqueous Electrolyte. *Chem. Rev.* **2019**, *119* (12), 7610–7672. https://doi.org/10.1021/acs.chemrev.8b00705.

(19) Kim, T.; Kumar, R. E.; Brock, J. A.; Fullerton, E. E.; Fenning, D. P. How Strain Alters CO_2 Electroreduction on Model Cu(001) Surfaces. *ACS Catal.* **2021**, *11* (11), 6662–6671. https://doi.org/10.1021/acscatal.0c05671.

(20) Liu, K.; Ma, M.; Wu, L.; Valenti, M.; Cardenas-Morcoso, D.; Hofmann, J. P.; Bisquert, J.; Gimenez, S.; Smith, W. A. Electronic Effects Determine the Selectivity of Planar Au–Cu Bimetallic Thin Films for Electrochemical CO_2 Reduction. *ACS Appl. Mater. Interfaces* **2019**, *11* (18), 16546–16555. https://doi.org/10.1021/acsami.9b01553.

(21) De Gregorio, G. L.; Burdyny, T.; Loiudice, A.; Iyengar, P.; Smith, W. A.; Buonsanti, R. Facet-Dependent Selectivity of Cu Catalysts in Electrochemical CO_2 Reduction at Commercially Viable Current Densities. *ACS Catal.* **2020**, *10* (9), 4854–4862. https://doi.org/10.1021/acscatal.0c00297.

(22) Feng, X.; Jiang, K.; Fan, S.; Kanan, M. W. A Direct Grain-Boundary-Activity Correlation for CO Electroreduction on Cu Nanoparticles. *ACS Cent. Sci.* **2016**, *2* (3), 169–174. https://doi.org/10.1021/acscentsci.6b00022.

(23) Bligaard, T.; Nørskov, J. K. Ligand Effects in Heterogeneous Catalysis and Electrochemistry. *Electrochimica Acta* **2007**, *52* (18), 5512–5516. https://doi.org/10.1016/j.electacta.2007.02.041.

(24) Hyman, M. P.; Medlin, J. W. Effects of Electronic Structure Modifications on the Adsorption of Oxygen Reduction Reaction Intermediates on Model Pt(111)-Alloy Surfaces. *J. Phys. Chem. C* **2007**, *111* (45), 17052–17060. https://doi.org/10.1021/jp075108g.

(25) Huang, J.; Dai, J.; Zhu, J.; Chen, R.; Fu, X.; Liu, H.; Li, G. Bimetallic Au-Cu Gradient Alloy for Electrochemical CO2 Reduction into C2H4 at Low Overpotential. *Journal of Catalysis* **2022**, *415*, 134–141. https://doi.org/10.1016/j.jcat.2022.09.033.

(26) Clark, E. L.; Hahn, C.; Jaramillo, T. F.; Bell, A. T. Electrochemical CO_2 Reduction over Compressively Strained CuAg Surface Alloys with Enhanced Multi-Carbon Oxygenate Selectivity. *J. Am. Chem. Soc.* **2017**, *139* (44), 15848–15857. https://doi.org/10.1021/jacs.7b08607.

(27) Tao, Z.; Wu, Z.; Yuan, X.; Wu, Y.; Wang, H. Copper–Gold Interactions Enhancing Formate Production from Electrochemical CO_2 Reduction. *ACS Catal.* **2019**, *9* (12), 10894–10898. https://doi.org/10.1021/acscatal.9b03158.

(28) Wang, X.; Ou, P.; Wicks, J.; Xie, Y.; Wang, Y.; Li, J.; Tam, J.; Ren, D.; Howe, J. Y.; Wang, Z.; Ozden, A.; Finfrock, Y. Z.; Xu, Y.; Li, Y.; Rasouli, A. S.; Bertens, K.; Ip, A. H.; Graetzel, M.; Sinton, D.; Sargent, E. H. Gold-in-Copper at Low *CO Coverage Enables Efficient Electromethanation of CO2. *Nat Commun* **2021**, *12* (1). https://doi.org/10.1038/s41467-021-23699-4.

(29) Feng, Y.; Yang, H.; Zhang, Y.; Huang, X.; Li, L.; Cheng, T.; Shao, Q. Te-Doped Pd Nanocrystal for Electrochemical Urea Production by Efficiently Coupling Carbon Dioxide Reduction with Nitrite Reduction. *Nano Lett.* **2020**, *20* (11), 8282–8289. https://doi.org/10.1021/acs.nanolett.0c03400.

(30) Chen, C.; Zhu, X.; Wen, X.; Zhou, Y.; Zhou, L.; Li, H.; Tao, L.; Li, Q.; Du, S.; Liu, T.; Yan, D.; Xie, C.; Zou, Y.; Wang, Y.; Chen, R.; Huo, J.; Li, Y.; Cheng, J.; Su, H.; Zhao, X.; Cheng, W.; Liu, Q.; Lin, H.; Luo, J.; Chen, J.; Dong, M.; Cheng, K.; Li, C.; Wang, S. Coupling N2 and CO2 in H2O to Synthesize Urea under Ambient Conditions. *Nat. Chem.* **2020**, *12* (8), 717–724. https://doi.org/10.1038/s41557-020-0481-9.

(31) Gerke, C. S.; Klenk, M.; Zapol, P.; Thoi, V. S. Pulsed-Potential Electrolysis Enhances Electrochemical C–N Coupling by Reorienting Interfacial Ions. *ACS Catal.* **2023**, *13* (22), 14540–14547. https://doi.org/10.1021/acscatal.3c03027.

(32) Liu, S.; Yin, S.; Wang, Z.; Xu, Y.; Li, X.; Wang, L.; Wang, H. AuCu Nanofibers for Electrosynthesis of Urea from Carbon Dioxide and Nitrite. *Cell Reports Physical Science* **2022**, *3* (5), 100869. https://doi.org/10.1016/j.xcrp.2022.100869.

(33) Nugraha, A. S.; Malgras, V.; Iqbal, M.; Jiang, B.; Li, C.; Bando, Y.; Alshehri, A.; Kim, J.; Yamauchi, Y.; Asahi, T. Electrochemical Synthesis of Mesoporous Au–Cu Alloy Films with Vertically Oriented Mesochannels Using Block Copolymer Micelles. *ACS Appl. Mater. Interfaces* **2018**, *10* (28), 23783–23791. https://doi.org/10.1021/acsami.8b05517.

(34) Yang, F.; Jiang, S.; Liu, S.; Beyer, P.; Mebs, S.; Haumann, M.; Roth, C.; Dau, H. Dynamics of Bulk and Surface Oxide Evolution in Copper Foams for Electrochemical CO2 Reduction. *Commun Chem* **2024**, *7* (1). https://doi.org/10.1038/s42004-024-01151-0.

(35) Timoshenko, J.; Roldan Cuenya, B. *In Situ*/*Operando* Electrocatalyst Characterization by X-Ray Absorption Spectroscopy. *Chem. Rev.* **2021**, *121* (2), 882–961. https://doi.org/10.1021/acs.chemrev.0c00396.

(36) Friebel, D.; Mbuga, F.; Rajasekaran, S.; Miller, D. J.; Ogasawara, H.; Alonso-Mori, R.; Sokaras, D.; Nordlund, D.; Weng, T.-C.; Nilsson, A. Structure, Redox Chemistry, and Interfacial Alloy Formation in Monolayer and Multilayer Cu/Au(111) Model Catalysts for CO_2 Electroreduction. *J. Phys. Chem. C* **2014**, *118* (15), 7954–7961. https://doi.org/10.1021/jp412000j.

(37) Guda, A. A.; Guda, S. A.; Lomachenko, K. A.; Soldatov, M. A.; Pankin, I. A.; Soldatov, A. V.; Braglia, L.; Bugaev, A. L.; Martini, A.; Signorile, M.; Groppo, E.; Piovano, A.; Borfecchia, E.; Lamberti, C. Quantitative Structural Determination of Active Sites from in Situ and Operando XANES Spectra: From Standard Ab Initio Simulations to Chemometric and Machine Learning Approaches. *Catalysis Today* **2019**, *336*, 3–21. https://doi.org/10.1016/j.cattod.2018.10.071.

(38) Bazin, D.; Rehr, J. J. Limits and Advantages of X-Ray Absorption Near Edge Structure for Nanometer Scale Metallic Clusters. *J. Phys. Chem. B* **2003**, *107* (45), 12398–12402. https://doi.org/10.1021/jp0223051.

(39) Timoshenko, J.; Lu, D.; Lin, Y.; Frenkel, A. I. Supervised Machine-Learning-Based Determination of Three-Dimensional Structure of Metallic Nanoparticles. *J. Phys. Chem. Lett.* **2017**, *8* (20), 5091–5098. https://doi.org/10.1021/acs.jpclett.7b02364.

(40) Timoshenko, J.; Halder, A.; Yang, B.; Seifert, S.; Pellin, M. J.; Vajda, S.; Frenkel, A. I. Subnanometer Substructures in Nanoassemblies Formed from Clusters under a Reactive Atmosphere Revealed Using Machine Learning. *J. Phys. Chem. C* **2018**, *122* (37), 21686–21693. https://doi.org/10.1021/acs.jpcc.8b07952.

(41) Wang, J.; Hsu, C.-S.; Wu, T.-S.; Chan, T.-S.; Suen, N.-T.; Lee, J.-F.; Chen, H. M. In Situ X-Ray Spectroscopies beyond Conventional X-Ray Absorption Spectroscopy on Deciphering Dynamic Configuration of Electrocatalysts. *Nat Commun* **2023**, *14* (1). https://doi.org/10.1038/s41467-023-42370-8.

(42) Kim, D.; Xie, C.; Becknell, N.; Yu, Y.; Karamad, M.; Chan, K.; Crumlin, E. J.; Nørskov, J. K.; Yang, P. Electrochemical Activation of CO_2 through Atomic Ordering Transformations of AuCu Nanoparticles. *J. Am. Chem. Soc.* **2017**, *139* (24), 8329–8336. https://doi.org/10.1021/jacs.7b03516.

(43) Guo, J.; Brimley, P.; Liu, M. J.; Corson, E. R.; Muñoz, C.; Smith, W. A.; Tarpeh, W. A. Mass Transport Modifies the Interfacial Electrolyte to Influence Electrochemical Nitrate Reduction. *ACS Sustainable Chem. Eng.* **2023**, *11* (20), 7882–7893. https://doi.org/10.1021/acssuschemeng.3c01057.

(44) Luo, Y.; Xie, K.; Ou, P.; Lavallais, C.; Peng, T.; Chen, Z.; Zhang, Z.; Wang, N.; Li, X.-Y.; Grigioni, I.; Liu, B.; Sinton, D.; Dunn, J. B.; Sargent, E. H. Selective Electrochemical Synthesis of Urea from Nitrate and CO2 via Relay Catalysis on Hybrid Catalysts. *Nat Catal* **2023**, *6* (10), 939–948. https://doi.org/10.1038/s41929-023-01020-4.

(45) Yang, G.-L.; Hsieh, C.-T.; Ho, Y.-S.; Kuo, T.-C.; Kwon, Y.; Lu, Q.; Cheng, M.-J. Gaseous CO_2 Coupling with N-Containing Intermediates for Key C–N Bond Formation during Urea Production from Coelectrolysis over Cu. *ACS Catal.* **2022**, *12* (18), 11494–11504. https://doi.org/10.1021/acscatal.2c02346.

(46) Carvalho, O. Q.; Marks, R.; Nguyen, H. K. K.; Vitale-Sullivan, M. E.; Martinez, S. C.; Árnadóttir, L.; Stoerzinger, K. A. Role of Electronic Structure on Nitrate Reduction to Ammonium: A Periodic Journey. *J. Am. Chem. Soc.* **2022**, *144* (32), 14809–14818. https://doi.org/10.1021/jacs.2c05673.

(47) Kuwabata, S.; Uezumi, S.; Tanaka, K.; Tanaka, T. Assimilatory and Dissimilatory Reduction of Nitrate and Nitrite with a Tris(Tetrabutylammonium) Nonakis(Benzenethiolato)Octasulfidohexaferratedimolybdate(3-) Modified Glassy-Carbon Electrode in Water. *Inorg. Chem.* **1986**, *25* (17), 3018–3022. https://doi.org/10.1021/ic00237a019.

(48) Wang, Z.; Richards, D.; Singh, N. Recent Discoveries in the Reaction Mechanism of Heterogeneous Electrocatalytic Nitrate Reduction. *Catal. Sci. Technol.* **2021**, *11* (3), 705–725. https://doi.org/10.1039/D0CY02025G.

(49) Ko, B. H.; Hasa, B.; Shin, H.; Zhao, Y.; Jiao, F. Electrochemical Reduction of Gaseous Nitrogen Oxides on Transition Metals at Ambient Conditions. *J. Am. Chem. Soc.* **2022**, *144* (3), 1258–1266. https://doi.org/10.1021/jacs.1c10535.

(50) Nørskov, J. K.; Abild-Pedersen, F.; Studt, F.; Bligaard, T. Density Functional Theory in Surface Chemistry and Catalysis. *Proc. Natl. Acad. Sci. U.S.A.* **2011**, *108* (3), 937–943. https://doi.org/10.1073/pnas.1006652108.

(51) Huang, H.; Russell, A. E. Approaches to Achieve Surface Sensitivity in the in Situ XAS of Electrocatalysts. *Current Opinion in Electrochemistry* **2021**, *27*, 100681. https://doi.org/10.1016/j.coelec.2020.100681.

(52) Huang, Y.-P.; Tung, C.-W.; Chen, T.-L.; Hsu, C.-S.; Liao, M.-Y.; Chen, H.-C.; Chen, H. M. *In Situ* Probing the Dynamic Reconstruction of Copper–Zinc Electrocatalysts for CO_2 Reduction. *Nanoscale* **2022**, *14* (25), 8944–8950. https://doi.org/10.1039/d2nr01478e.

(53) Velasco-Vélez, J.-J.; Jones, T.; Gao, D.; Carbonio, E.; Arrigo, R.; Hsu, C.-J.; Huang, Y.-C.; Dong, C.-L.; Chen, J.-M.; Lee, J.-F.; Strasser, P.; Roldan Cuenya, B.; Schlögl, R.; Knop-Gericke, A.; Chuang, C.-H. The Role of the Copper Oxidation State in the Electrocatalytic Reduction of CO_2 into Valuable Hydrocarbons. *ACS Sustainable Chem. Eng.* **2019**, *7* (1), 1485–1492. https://doi.org/10.1021/acssuschemeng.8b05106.

The data supporting this article have been included as part of the Supplementary Information. Additional data is available upon request.